






# Influence of the Synthesis Route on the Structural and Magnetic Properties of $\text{La}_{0.7}\text{Sr}_{0.3}\text{MnO}_3$ Nanoparticles

## Influencia de la ruta de síntesis en las propiedades estructurales y magnéticas de nanopartículas de $\text{La}_{0.7}\text{Sr}_{0.3}\text{MnO}_3$

Jenny A. Mera-Córdoba <sup>1</sup>, Jhon F. Betancur-Pérez <sup>2</sup>, Nicolás A. Salazar-Henao <sup>3</sup>  
Luis Alejandro Galeano <sup>4</sup> Andrés Rosales-Rivera <sup>5</sup>, and Diego F. Coral-Coral <sup>6</sup>

### ABSTRACT

Cancer is one of the leading causes of death worldwide, significantly impacting public health, with current treatment options that often have side effects on patients. In this context, magnetic hyperthermia emerges as a non-invasive alternative that utilizes magnetic nanoparticles to generate heat and destroy cancer cells. In this vein, this research sought to synthesize magnetic  $\text{La}_{0.7}\text{Sr}_{0.3}\text{MnO}_3$  (LSMO) nanoparticles in order to study the effect of the synthesis route on the production of nanoparticles with optimal properties for biomedical applications. LSMO samples were synthesized via the sol-gel, ceramic, and Pechini methods. These samples were characterized through X-ray diffraction (XRD), small-angle X-ray scattering (SAXS), thermogravimetric analysis (TGA), and vibrating sample magnetometry (VSM) in order to study their structure, morphology, and magnetic behavior. The nanoparticles obtained via the Pechini method exhibited the best crystalline structure, the smallest size, and reduced magnetic properties. This work allowed identifying the ceramic method as the synthesis route that produces nanoparticles suitable for biomedical applications, as demonstrated through the numerical calculation of the specific absorption rate (SAR). The results indicated that the SAR of nanoparticles synthesized using this method is 30 times greater than that of samples synthesized using the other two methods under equal field amplitude and frequency conditions.

**Keywords:** ceramic synthesis, hyperthermia applications, manganites, Pechini synthesis, sol-gel synthesis

### RESUMEN

El cáncer es una de las principales causas de muerte a nivel mundial y tiene un impacto significativo en la salud pública, con opciones de tratamiento actuales que suelen generar efectos secundarios en los pacientes. En este contexto, la hipertermia magnética surge como una alternativa no invasiva que utiliza nanopartículas magnéticas para generar calor y destruir células cancerígenas. Dado lo anterior, esta investigación buscó sintetizar nanopartículas magnéticas de  $\text{La}_{0.7}\text{Sr}_{0.3}\text{MnO}_3$  (LSMO) para estudiar el efecto de la ruta de síntesis en la producción de nanopartículas con propiedades óptimas para aplicaciones biomédicas. Las muestras de LSMO fueron sintetizadas mediante los métodos sol-gel, cerámico y Pechini. Estas muestras fueron caracterizadas mediante difracción de rayos X (XRD), dispersión de rayos X a bajo ángulo (SAXS), análisis termogravimétrico (TGA) y magnetometría de muestra vibrante (VSM), con el fin de estudiar su estructura, morfología y comportamiento magnético. Las nanopartículas obtenidas mediante el método Pechini presentaron la mejor estructura cristalina, el menor tamaño y propiedades magnéticas reducidas. Este trabajo permitió identificar el método cerámico como la ruta de síntesis que produce nanopartículas adecuadas para aplicaciones biomédicas, como se demostró mediante el cálculo numérico de la tasa específica de absorción (SAR). Los resultados indicaron que el SAR de las nanopartículas sintetizadas con este método es 30 veces mayor que el de las muestras sintetizadas mediante los otros dos métodos bajo iguales condiciones de amplitud de campo y frecuencia.

**Palabras clave:** aplicaciones de hipertermia, manganitas, síntesis cerámica, síntesis sol-gel, síntesis Pechini

**Received:** August 16<sup>th</sup>, 2024

**Accepted:** May 19<sup>th</sup>, 2025

<sup>1</sup> PhD(c) in Sustainable Development, Universidad de Manizales, Colombia. MSc in Sustainable Development and Environment, Universidad de Manizales, Colombia. PhD Fellow, Ministry of Science, Technology, and Innovation (Min-ciencias). Affiliation: Research Group in Nanostructured Functional Materials, Universidad CESMAG, Colombia. Email: jennyalmc@gmail.com

<sup>2</sup> PhD in Agricultural Science, Universidad Nacional de Colombia. Affiliation: Research professor, Universidad de Manizales, Colombia. E-mail: jbetancur@umanizales.edu.co

<sup>3</sup> MSc in Physics, Universidad Nacional de Colombia, Colombia. Affiliation: Magnetism and Advanced Materials Laboratory, Universidad Nacional de Colombia, Manizales campus, Manizales, Colombia. E-mail: nashenao@gmail.com

<sup>4</sup> PhD in Inorganic Chemistry and Chemical Reactivity, University of Salamanca, Spain. Affiliation: Functional Materials and Catalysis Research Group (GIMFC), Universidad de Nariño, Colombia. E-mail: luis.alejandrogaleano@gmail.com

<sup>5</sup> PhD in Physics, Universidade Federal de Pernambuco, Brazil. Affiliation: Magnetism and Advanced Materials Laboratory, Universidad Nacional de Colombia, Manizales campus, Manizales, Colombia. E-mail: arosalesr@unal.edu.co

<sup>6</sup> PhD in Physics, Universidad Nacional de La Plata, Argentina. Affiliation: Research Group in Science and Technology of Ceramic Materials, Department of Physics, Universidad del Cauca, Colombia. Email: dfcoral@unicauca.edu.co



Attribution 4.0 International (CC BY 4.0) Share - Adapt

## Introduction

It is well known that particle size, morphology, and crystalline homogeneity influence the properties of materials at the nanometric scale. In the case of manganites such as  $\text{La}_{1-x}\text{Sr}_x\text{MnO}_3$  (LSMO), these properties can be modified through different synthesis techniques. Particularly, particle size can be controlled using different synthesis methods and processing conditions [1]–[4].

The properties of LSMO that depend on particle size are critical for biomedical applications, e.g., saturation magnetization ( $M_s$ ), and it has been demonstrated that particle size range influences the magnetic response [1], [5]. Thus, the specific absorption rate (SAR), a key parameter for magnetic hyperthermia applications of nanoparticles, is directly proportional to  $M_s^2$  [6], [7]. Likewise, particle heating efficiency can be used to activate thermo-sensitive polymers for drug delivery applications [8], [9]. In magnetic imaging diagnosis, particle size also plays an important role in relation to the longitudinal and transverse relaxation times [10]. In addition, improving the magnetic properties of LSMO nanoparticles, as well as coating them with carboxyl-containing polymers such as PVA, opens new possibilities for use in RNA extraction by magnetic separation, contributing to the diagnosis of viral agents such as SARS-CoV-2, as recently proposed by [11].

Most of these applications have employed iron oxide magnetic nanoparticles (IOMNPs) such as  $\text{Fe}_3\text{O}_4$  and  $\gamma\text{-Fe}_2\text{O}_3$ . Several works have demonstrated that nanoparticles with a lower Curie temperature favor heating in the therapeutic range (41–47 °C) for magnetic hyperthermia applications [12]–[15]. Typical IOMNPs exhibit a Curie temperature of around 858 K [14], [16], while manganite nanoparticles ( $\text{La}_{1-x}\text{Sr}_x\text{MnO}_3$ ) fall within the range of 350–370 K [15]. This can be tuned by means of the Sr content [17]–[19], which makes LSMO a promising family of compounds for biomedical applications.

Lanthanum manganites ( $\text{LaMnO}_3$ ) are complex manganese oxides with a perovskite-like crystalline structure, which can be understood as a set of regular  $\text{MnO}_6$  octahedra in contact with each other through their vertices. In this structure, oxygen ions are located at the vertices, while La occupies the center of the cube. When  $\text{La}^{3+}$  ions are partially replaced by divalent ions such as  $\text{Sr}^{2+}$  in a specific proportion, LSMO perovskite is formed, and a double exchange interaction between  $\text{Mn}^{3+}$  and  $\text{Mn}^{4+}$  ions takes place, favoring the change in crystalline phase from an orthorhombic structure (Pbnm) to a rhombohedral one (R3c) [4], [20]–[22], with the latter being responsible for the structural, electrical, and magnetic properties of LSMO [23], [24].

The use of LSMO nanoparticles in magnetic hyperthermia is possible due to their biocompatibility. Several studies on these nanoparticles have revealed a low cytotoxicity, making them suitable for biomedical applications, particularly for magnetic hyperthermia. *In vitro* cytotoxicity tests conducted

on HeLa cell lines using MTT assays demonstrated a concentration-dependent effect, with approximately 92% cell viability at 1 mg/mL and 63% at 5 mg/mL, suggesting minimal toxicity at lower concentrations [25]. This low cytotoxicity can be attributed to the hydroxyl group coating on the nanoparticles, which enhances their biocompatibility. Similar results were reported using concentrations of 0.66, 0.9, and 1.02 mg/mL after 96 hours, demonstrating that LSMO nanoparticles significantly reduce cell viability in a time- and dose-dependent manner; the viability decreased by 69, 82, and 86%, respectively [26]. Likewise, LSMO nanoparticles, particularly those with silica coatings, have shown promising biocompatibility and controlled cytotoxicity, which makes them suitable for magnetic hyperthermia cancer therapy. *In vitro* biocompatibility assessments using murine fibroblast (L929) cells indicated a high viability, exceeding 70% at 1 mg/mL and reaching over 93% at 250  $\mu\text{g/mL}$ , which again confirms these nanoparticles' minimal toxicity at lower concentrations [27].

This work analyzes the influence of synthesis pathways on the magnetic and morphological properties of LSMO nanoparticles. Additionally, it explores how these properties affect heat generation in radiofrequency fields, with the aim of proposing LSMO nanoparticles as heat mediators in hyperthermia experiments for cancer treatment. Studies on magnetic nanoparticles (MNPs) with a LSMO perovskite-type structure in the field of hyperthermia are still scarce, which justifies further exploration.

To this effect, three different synthesis methods, including the traditional sol-gel process [28], the ceramic method [29], and the Pechini method [30, 31] were employed to prepare LSMO nanoparticles. In the ceramic method, the metal oxides or carbonates are used as precursors, which are mixed and calcined at high temperatures to form nanoparticles. Generally, the resulting compounds have an inhomogeneous size distribution and impurity phases [29]. In wet chemical approaches like the Pechini and sol-gel methods, the formation of nanoparticles occurs during the decomposition of previously formed organic-inorganic complexes. These processes provide smaller nanoparticles, along with a better control of stoichiometry, size, and morphology as well as fewer defects [32]. Once the nanoparticles had been characterized, we analyzed the influence of these synthesis methods on their structural, morphological, and magnetic properties.

To bridge the knowledge gap between LSMO nanoparticles and their potential biomedical applications, we performed a morphological, structural, and magnetic characterization of synthesized LSMO nanoparticles, with the aim of identifying the method that offers the most homogeneous LSMO nanoparticles as well as improved magnetic properties.

This document is organized as follows. In the *Experimentation* section, the methods used are presented. The *Results and discussion* section outlines the results and correlates the properties obtained. This section is divided into structural,

thermal, and magnetic characterization, concluding with specific absorption rate (SAR) simulations to examine the application of LSMO nanoparticles in hyperthermia. Finally, the main conclusions of this work are presented.

## Experimentation

### Synthesis methods

#### Pechini's method

Citric acid and ethylene glycol (1:4 molar ratio) were initially mixed for 30 min under constant stirring at 80 °C in a reflux system. Subsequently, high purity nitrates were added in a 1:1 molar ratio (citrate:cation), i.e.,  $\text{La}(\text{NO}_3)_3 \cdot 6\text{H}_2\text{O}$  (99.99%),  $\text{Sr}(\text{NO}_3)_2 \cdot 6\text{H}_2\text{O}$  (99.9 %) and  $\text{Mn}(\text{NO}_3)_2 \cdot 6\text{H}_2\text{O}$  (99.9 %), which had been previously dissolved in water, and heated at 80 °C for an additional 30 min. Once a pH of 5.0 was reached, it was maintained by adding  $\text{NH}_4\text{OH}$ . Esterification was performed in an electric oven at 140 °C, which, in turn, enabled the removal of traces of  $\text{H}_2\text{O}$ . The result was heated to 180 °C to remove the excess of ethylene glycol released during polymerization and oligomerization. The obtained solid was then calcined at 250 °C for 8 h. Finally, the powders were calcined at 650 °C for 12 h [33]. The sample synthesized through this method was labeled as M1.

#### Ceramic method

In this method,  $\text{La}_2\text{O}_3$  (99.99%),  $\text{Sr}(\text{NO}_3)_2 \cdot 6\text{H}_2\text{O}$  (99.9%), and  $\text{MnO}_2$  (99%) precursors were mixed in stoichiometric quantities and grinded in agate mortar for 45 min. The obtained powders were calcined in a muffle at 1100 °C for 12 h, with subsequent sintering at the same temperature for an additional 12 h [34]. The sample synthesized by this route was labeled as M2.

#### Sol-gel method

In the sol-gel synthesis of LSMO nanoparticles, the required molar amounts of the metal salts  $\text{La}(\text{NO}_3)_3 \cdot 6\text{H}_2\text{O}$  (99.99%),  $\text{Sr}(\text{NO}_3)_2 \cdot 6\text{H}_2\text{O}$  (99.9%), and  $\text{Mn}(\text{NO}_3)_2 \cdot 6\text{H}_2\text{O}$  (99.9 %) were dissolved in bi-distilled water, and then a mixture of citric acid:ethylene glycol (1:4) was added to the solution. The molar ratio between the salts and the mixture was 1:10. The solution was heated to 80 °C under vigorous stirring until a polymer gel was formed as a result of the poly-esterification reaction, which was then pyrolyzed at 200 °C. The obtained powder was further heated at 400 °C for 2 h and at 650 °C for 12 h [24], [35]. This solid was labeled as M3.

### Structural, morphologic, and magnetic characterization

The structural properties of the LSMO powders were studied using X-ray diffraction (XRD). The samples were irradiated with Cu K $\alpha$  radiation ( $\lambda=1.5406$  Å) from an

X-ray source powered at constant voltage (40 kV) and constant current (40 mA). Diffraction data were acquired with a LynxEye linear detector in a  $2\theta$  range of 2.000-69.999°, with a step of 0.024°. A qualitative analysis by comparison with the PDF-2(2016) diffraction dataset was conducted, and a quantitative analysis was carried out by fitting the observed diffraction patterns with the inorganic crystal structure database (ICSD) by means of the Rietveld method. The reported percentages correspond to the relationship between the polycrystalline phases, quantified without considering any content of amorphous material. Additionally, the crystal size ( $d_{\text{XRD}}$ ) was estimated from XRD data via the Scherrer equation.

Particle size and morphology were studied using small-angle X-ray scattering (SAXS). To this effect, SAXS patterns were obtained in the National Synchrotron Light Laboratory at Campinas, Brazil. The powder samples were sealed with Kapton tape into a 1 mm wide sample holder. For the SAXS measurements, the samples were illuminated with monochromatic X-ray radiation ( $\lambda=1.489$  Å), and the resulting 2-D scattering patterns were recorded using a MAR165-CCD camera. To achieve a  $q$ -range of 0.14-5.09  $\text{nm}^{-1}$  a sample-detector length of 878.8 mm was used. An empty sample holder was also measured in order to subtract the Kapton contribution to the sample's scattering.

The obtained SAXS patterns were fitted using the mathematical model for the scattered intensity ( $I$ ) of spherical particles as a function of the wave vector ( $q$ ), as expressed in Eq. (1).

$$I(q) = \int_0^\infty f(r) F^2(r, q, \Delta\eta) dr + I_B \quad (1)$$

where  $f(r)$  is the lognormal size distribution of primary particles of radius  $r$ , characterized by the median radius ( $r_o$ ) and the standard deviation ( $\sigma$ ) for the Gaussian distribution of the variable  $u = \ln(r/r_o)$ .

$F(r, q, \Delta\eta)$  is the spherical form factor [36] that represents the scattering amplitude produced by spherical particles of radius  $r$ , as given in Eq. (2)

$$F(r, q, \Delta\eta) = 4\pi r^3 \Delta\eta \left( \frac{\sin(qr) - qr \cos(qr)}{(qr)^3} \right) \quad (2)$$

where  $\Delta\eta$  is the electronic contrast difference between the particle and the matrix, and  $I_B$  is the background intensity. From the fitted parameters ( $r_o$  and  $\sigma$ ), the mean particle radius ( $R_{\text{SAXS}} = r_o e^{\sigma^2/2}$ ) and the standard deviation ( $sd = R_{\text{SAXS}} \sqrt{\sigma^2 - 1}$ ) were calculated. Note that the fitting processes were carried out using SASfit software [37].

Thermal stability was assessed by means of thermogravimetric analysis (TGA) curves using a TA Instruments TGA-Q500. The equipment was previously calibrated using the Curie temperature of a nickel sample (99.99% purity). In order to



avoid oxidation during the thermal process, the oven was previously purged with a constant flux of nitrogen for 30 min. For thermal decomposition analysis, the sample mass was measured throughout the temperature ramp (from 25 to 800 °C) at a constant rate of 5 °C/min under a nitrogen atmosphere (60 mL/min flux).

The magnetic characterization of each sample was carried out using a vibrating sample magnetometer (VSM-VersaLab by Quantum Design). Isothermal specific magnetization ( $M$ ) loops under an applied magnetic field ( $H$ ) with a maximum  $H$  of 3.0 T for different temperatures were taken from a known mass of powder samples. The selected temperatures ranged between 50 and 325 K. For magnetization cycles analysis, the particle mean magnetic moment ( $\langle\mu\rangle$ ), the saturation magnetization ( $M_s$ ), and coercive field ( $H_c$ ) were calculated.

A flowchart of our methodology is presented in Fig. 1.

## Results and discussion

### XRD and SAXS analyses

The XRD patterns are shown in Fig. 2a. For all samples, the most intense diffraction peaks were indexed for a rhombohedral structure with the space group R3, corresponding to the crystalline structure of  $\text{La}_{1-x}\text{Sr}_x\text{MnO}_3$  [1]–[3].

The quantitative analysis performed using the Rietveld method revealed that the main perovskite crystal phase was  $\text{La}_{0.7}\text{Sr}_{0.3}\text{MnO}_3$  for samples M1 and M3 (74.2 and 30.6%). The diffraction peaks can be indexed using a cubic crystalline structure. The calculated lattice parameters were  $a = 5.50(9)$  Å,  $5.52(1)$  Å, and  $5.56(6)$  Å for samples M1, M2, and M3, respectively. Other crystalline phases for M1 included  $x = 0.33$  (21.4%) and  $x = 0.4$  (4.4%). As reported in the literature [37], [38], a lower incidence of undesired crystalline phases might even be achieved through longer sintering at the same synthesis temperature. For sample M2, the phase corresponding to  $x =$

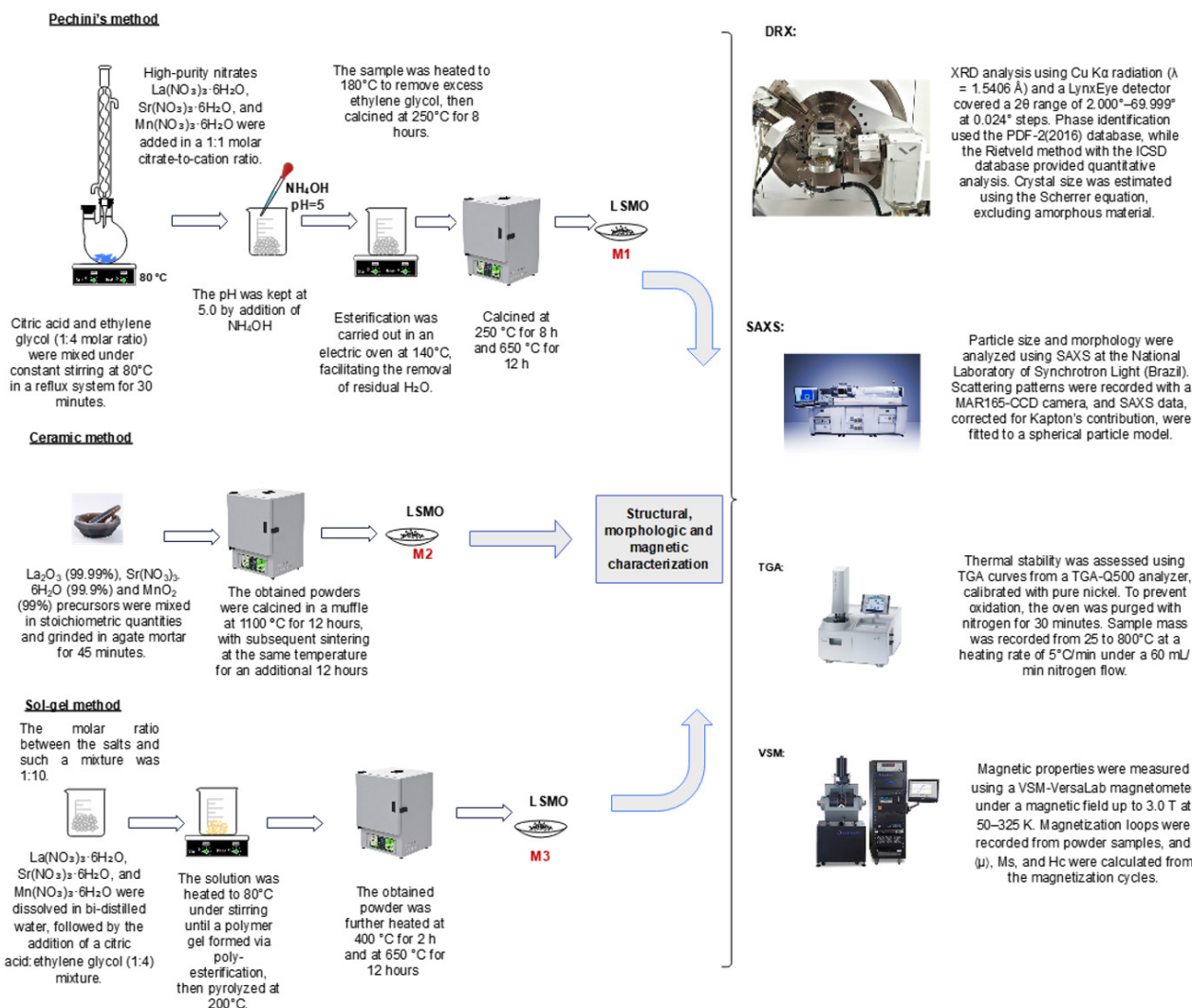


Figure 1. Methodology flowchart

Source: Authors

0.3 was not observed, and the main crystalline phase was  $x = 0.33$  (38.5%). For this sample, precursors and intermediate compounds such as  $\text{La}(\text{MnO}_3)$  (27.1%) and  $\text{La}(\text{OH})_3$  (15.2%) were observed alongside Sr and La silicates (20.2 %). In Fig. 2b, the diffraction peaks for  $\text{La}(\text{MnO}_3)$ ,  $\text{La}(\text{OH})_3$ , and the silicates are labeled with +, o, and \*, respectively.

In the case of sample M3,  $\text{Sr}(\text{CO}_3)$  (32.4%) and  $\text{LaSr}_4\text{Mn}_5\text{O}_{13}$  (37.0%) were observed. In Fig. 2c, the diffraction peaks for  $\text{Sr}(\text{CO}_3)$  are labeled with arrows.

The above indicates that the best synthesis procedure to obtain  $\text{La}_{0.7}\text{Sr}_{0.3}\text{MnO}_3$  was the Pechini method (M1). Sample M3, synthesized via the sol-gel method, reported a low reaction yield and low crystallinity, which can be attributed to the fact that the pH of the reaction was not controlled.

Some studies have stated that the homogeneity and stability of metal citrate solutions may largely depend on the pH, which is particularly important in systems with several different metals. This is useful in optimizing the formation of stable species of metal citrate and avoiding the precipitation of individual hydroxides [39], [40]. This parameter is relevant in controlling the sample particle size [41].

Once the samples had been structurally analyzed, SAXS was used to prove whether the samples were composed of particles in the nanometric range. The measured SAXS patterns, the curves fitted using Eq. (1), and the best-fitted particle mean size ( $R_{\text{SAXS}}$ ) and size standard distribution (s.d) values are shown in Fig. 2 and Table I.

The SAXS curve fitting revealed that the spherical model was sufficient to fit all the data. The wide size distribution obtained from the fitting is presented in the form of insets in Fig. 3 (b, c, d), indicating a polydispersity of over 55% for samples M1 and M3, as well as over 93% for sample M2. The mean radius ( $R_{\text{SAXS}}$ ) is in agreement with the crystal size ( $d_{\text{XRD}}$ ) measured using the XRD peak at  $32.7^\circ$  and the Scherrer equation – if each crystal is assumed to be a sphere of diameter  $d_{\text{XRD}}$ .

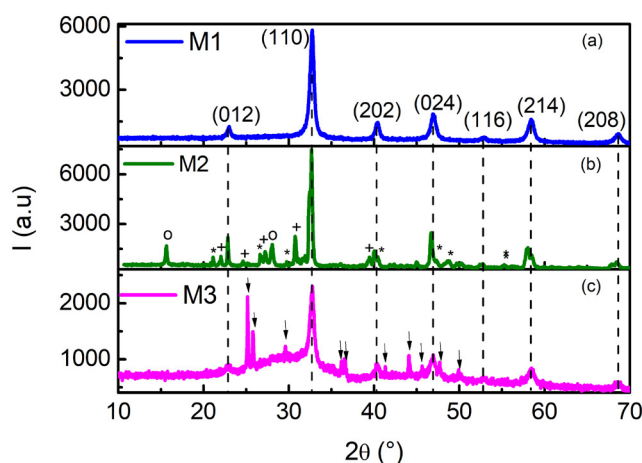


**Figure 2.** X-ray diffraction patterns for all the samples. The indexed peaks are related with the  $\text{La}_{0.7}\text{Sr}_{0.3}\text{MnO}_3$  crystalline structure.

Source: Authors

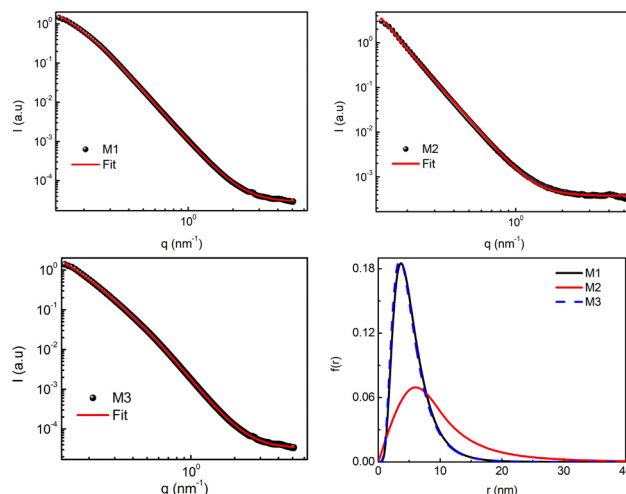


**Figure 3.** SAXS pattern for samples M1, M2, and M3. Solid lines correspond to the best-fit curves obtained using Eq. (1). The particle number size distribution obtained via the SAXS fitting procedure is also presented.

Source: Authors

### Thermal degradation

TGA curves are shown in Fig. 4. These analyses were performed on the final products after calcination. Fig. 3a presents the percent mass loss vs. the temperature for all the samples.

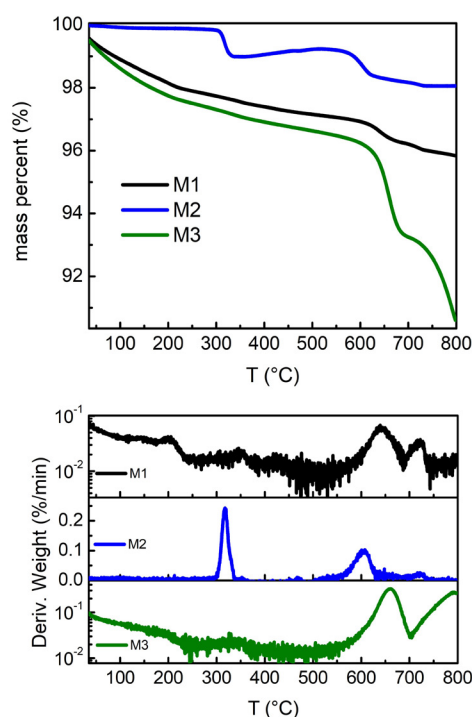


**Figure 4.** Thermal decomposition of all samples. a) Mass loss curves. Arrows indicate the two main thermal decomposition processes. b) Differential mass loss curves.

Source: Authors

In this figure, sample mass losses take place as the temperature increases. For samples M1 and M3, two different thermal events are observed (indicated with arrows in Fig. 3a). First, a slight mass reduction between room temperature and 550 °C, followed by an abrupt mass loss between 550 and 700 °C. This second reduction is clearly more pronounced for sample M3. Meanwhile, sample M2 exhibits an abrupt mass reduction between 250 and 300 °C, as well as a second reduction in the range of 550 to 650 °C. In Fig. 4b, these stages are more clearly seen as peaks, whose centers correspond to the mean decomposition temperatures.

The observed thermal behavior is related to the chemical composition of the samples, considering that each chemical phase decomposes at a different temperature. Hence, the initial slight mass loss of samples M1 and M3 may be associated with sample dehydration.

In Fig. 5, the second derivative of the TGA curve ( $d^2W/dT^2$ ) serves as a powerful analytical tool that enhances the resolution of thermal events by revealing inflection points not readily apparent in the original or first-derivative data [42]. For all the samples, the second derivative exhibits multiple transitions corresponding to distinct decomposition steps, indicating the breakdown of the material into several subphases. These subtle changes provide a precise delineation of the onset, peak, and termination temperatures of each thermal event, allowing for a more comprehensive understanding of the material's thermal stability and compositional complexity. The rapid drop in the second derivative at the onset of the first decomposition event (25-100 °C) indicates a sudden, pronounced change in the reaction kinetics, consistent with the beginning of thermal decomposition. This behavior suggests that a specific subphase, which is less thermally stable, undergoes an abrupt breakdown, leading to a swift acceleration of the mass loss rate, typically associated with physisorbed water. Essentially, it marks a well-defined thermal event where the material's structure rapidly transitions from a stable state to a decomposing phase, highlighting the onset of a critical degradation step [43].

In Fig. 4b, a peak related to the thermal decomposition of unreacted precursors [44], [45] was observed for all the samples between 250 and 300 °C. For sample M2, this peak was more pronounced, and the mass loss corresponded to 1.0%. In samples M1 and M3, although this peak was also observed, the mass loss was rather negligible. This correlates well with the unreacted precursors observed via XRD for sample M2. The peak observed between 550 and 700 °C corresponds to the thermal decomposition of organic remnants from the synthesis process [2]. In this stage, mass losses of 2.3, 0.9, and 7.1 were recorded for samples M1, M2, and M3, respectively. The mass percentages after the thermal process were 95.85, 98.05, and 90.61% for samples M1, M2, and M3, which could correspond to dehydrated LSMO nanoparticles [2].

## Magnetic properties

Fig. 6 shows the magnetization curves at different temperatures for each sample. The magnetization ( $M$ ) was normalized using the  $\text{La}_{1-x}\text{Sr}_x\text{MnO}_3$  phases (LSMO) present in each sample according to the XRD analyses. This value increased with the magnetic field ( $H$ ) until saturation was reached ( $M_s$ ). Likewise, the saturation decreased when the temperature increased, as expected for magnetic systems [1], [5]. The insets in Fig. 4 show the coercive field ( $H_c$ ) for each temperature. As expected, the coercive field did tend to zero when the temperature increased [46].

Fig. 6d presents the magnetization curves at 300 K. These curves were fitted using the Langevin equation convoluted with a lognormal distribution of magnetic moments ( $f(\mu)$ ):

$$M = \int_0^\infty N\mu \left[ \text{Coth} \left( \frac{\mu\mu_o H}{k_B T} \right) - \frac{k_B T}{\mu\mu_o H} \right] f(\mu) d\mu + \chi_{par} H \quad (3)$$

In this model,  $\mu$  is the particle magnetic moment,  $N$  is the mass density of magnetic moments,  $\chi_{par}$  represents the susceptibility associated with paramagnetic contributions to the magnetization process, and  $\mu_0 = 4\pi \times 10^{-7} \text{ Tm/A}$  denotes the vacuum magnetic permeability.

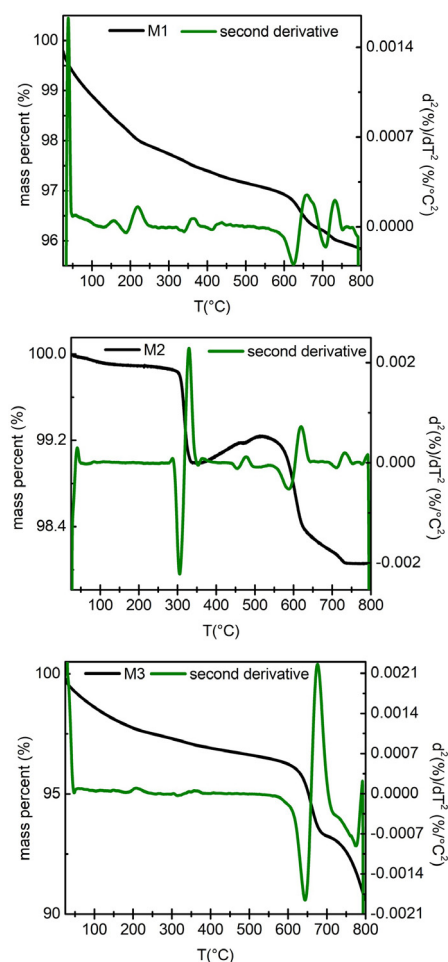
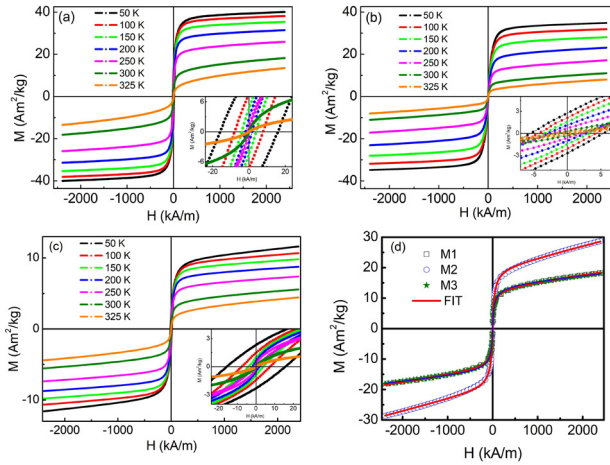


Figure 5. Second-derivative analysis of TGA curves

Source: Authors





**Figure 6.** M vs. H curves at different temperatures, measured by means of VSM, for samples a) M1, b) M2, and c) M3. Insets: zoom around the zero-field. d) Magnetization curve at 300 K for samples M1, M2, and M3. Continuous lines represent best-fit curve obtained using Eq. (3).

**Source:** Authors

From the fittings, the magnetic saturation was calculated as  $M_s = N\langle\mu\rangle$ , where  $\langle\mu\rangle$  is the mean magnetic moment calculated from the fitted lognormal distribution  $f(\mu)$ . The results showed that the 300 K magnetization curves can be fully fitted using Eq. (3), which indicates that, at 300 K, the LSMO nanoparticles behaved as super-paramagnetic [47].

The fitted  $\langle\mu\rangle$  and  $M_s$  values are presented in Table 1. Both parameters were similar for samples M1 and M3. For sample M2,  $\langle\mu\rangle$  was around 1.6 times the value obtained for M1. This value was equal to the ratio between the crystallite volumes of samples M1 and M2, which indicates that, the higher the particle size, the higher the magnetic moment. This behavior has already been observed for similar  $\text{La}_{0.7}\text{Sr}_{0.3}\text{MnO}_3$  nanoparticles [48]. Eq. (3) was also used to determine  $M_s$  and  $H_c$  for each temperature.

The fitting procedure was enough to fit the curve, even for the lowest temperature. In order to determine the coercive field from the fittings, the Langevin equation was displaced for  $\pm H_c$ . This value corresponds to a fitting parameter.

**Table 1.** Structural, morphological, and magnetic parameters of the samples. Here,  $d_{\text{XRD}}$  is the crystallite size obtained from X-ray diffraction,  $R_{\text{SAXS}}$  is the mean particle radius (with a standard distribution s.d.) obtained from SAXS,  $\langle\mu\rangle$  is the mean particle magnetic moment (with a standard distribution s.d.),  $M_s$  is the magnetic saturation,  $H_c$  is the coercive field,  $T_B$  is the magnetic blocking temperature,  $K_{\text{eff}}$  is the magnetic anisotropy constant,  $M_0$  is the magnetic saturation extrapolated to 0 K, and  $T_c$  is the Curie temperature.

Sample	$d_{\text{XRD}}$ (nm)	$R_{\text{SAXS}} \pm \text{sd}$ (nm)	$\langle\mu\rangle \pm \text{sd}$ ( $\mu_B$ )	$M_s$ ( $\text{Am}^2/\text{kg}_{\text{LSMO}}$ )	$H_c$ (kA/m)	$T_B$ (K)	$K_{\text{eff}}$ ( $\text{J}/\text{m}^3$ )	$M_0$ ( $\text{Am}^2/\text{kg}_{\text{LSMO}}$ )	$\alpha$	$T_c$ (K)
M1 Pechini	$14.5 \pm 0.7$	$5.4 \pm 3.0$	$6570 \pm 42$	$13.6 \pm 0.9$	0	$189 \pm 18$	$11175 \pm 1281$	$40.3 \pm 0.6$	$2.49 \pm 0.02$	$358 \pm 28$
M2 Ceramic	$17.0 \pm 0.7$	$8.2 \pm 7.7$	$10534 \pm 550$	$19.8 \pm 0.1$	$1.45 \pm 0.04$	$458 \pm 4$	$2740 \pm 27$	$89.7 \pm 2.5$	$1.22 \pm 0.06$	$353 \pm 123$
M3 Sol-gel	$14.6 \pm 0.7$	$5.3 \pm 3.0$	$6690 \pm 77$	$14.4 \pm 0.6$	$0.27 \pm 0.01$	$186 \pm 20$	$11168 \pm 1574$	$33.6 \pm 0.5$	$2.71 \pm 0.02$	$367 \pm 28$

**Source:** Authors

Fig. 7 presents the thermal behavior of the coercive field and the magnetic saturation. In Fig. 7a, the behavior of  $H_c$  vs.  $T^{1/2}$  is shown. The coercive field decreased with temperature until a value of zero was reached. For superparamagnetic nanoparticles, a linear behavior is expected – it is observed at lower temperatures. The theoretical temperature at which  $H_c = 0$  is known as the *blocking temperature* ( $T_B$ ). When  $T > T_B$ , nanoparticles are expected to behave as superparamagnetic particles, and, when  $T < T_B$ , the magnetic anisotropy energy is higher than the thermal energy. Then, the thermal fluctuation ceases, and the particles' magnetic moments become blocked.

The  $H_c$  vs.  $T^{1/2}$  curves were fitted using the thermal-activated Stoner-Wohlfarth model [49]–[51]:

$$H_c = H_k \left( 1 - \left( \frac{T}{T_B} \right)^{1/2} \right) \quad (4)$$

In Eq. (4),  $H_k = 0.96 \frac{K_{\text{eff}}}{\mu M_{s0K}}$  is the anisotropy field,  $K_{\text{eff}}$  is the effective magnetic anisotropy constant,  $\mu$  denotes the particle magnetic moment,  $M_{s0K}$  is saturation magnetization at  $T = 0$  K, and  $T_B$  is the blocking temperature. It has been demonstrated that this method enables a good approximation to the blocking temperature [7],[52].

The fitted values of  $T_B$  and  $K_{\text{eff}}$  are shown in Table 1. They are in good agreement with those measured for similar nanoparticles [48], [53], [54]. In Fig. 7b, the fitted  $M_s$  is plotted against temperature. For all the samples,  $M_s$  decreased with temperature. This behavior is typical of ferromagnetic materials. The temperature at which  $M_s = 0$  is called the *Curie temperature* ( $T_c$ ). In order to obtain information from the  $M_s$  vs.  $T$  curves, these values were fitted using the spin-wave model for the dependence of  $M_s$  on the temperature  $T$  [55]:

$$M_s(T) = M_0 (1 - B_0 T^\alpha) \quad (4)$$

where  $M_0$  is the saturation magnetization at 0 K and  $B_0$  is a constant whose value depends on the exchange integral  $J$ . The coefficient  $\alpha$  generally takes the value of 3/2 for bulk

ferromagnetic materials and, for some bulk spinel ferrites,  $\alpha$  ranges between 0.2 and 2.0. The fitted values for  $M_0$  and  $\alpha$  are presented in Table 1 and the best-fit curves are shown in Fig. 7b.

The fitted value for  $M_0$  was similar for samples M1 and M3, and the value of  $M_0$  found for sample M2 was similar to those reported for larger particles [42], [56]. The lower magnetization of samples M1 and M3 could be related to the formation of a magnetically frustrated layer on the particle's surface – these effects were more marked when the particle size was reduced [57].

The fitted  $\alpha$  values were 2.49 for M1, 1.22 for M2, and 2.71 for M3. It has been demonstrated that the  $\alpha$  value depends on particle size: the smaller the size, the higher the  $\alpha$  value [48]. This was confirmed via XRD and SAXS size analysis: M2 exhibited the highest mean particle size in comparison with M1 and M3. The  $\alpha$  value fitted for sample M2 was the nearest to  $\alpha = 3/2$ , indicating that the particles almost reached the bulk state.

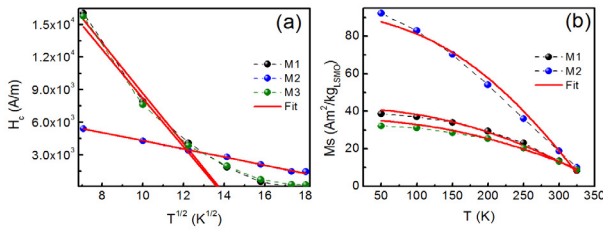


**Figure 7.** Thermal behavior of a) the coercive field ( $H_c$ ) and b) the magnetic saturation

**Source:** Authors

From the fittings, the value of  $T_c$  was calculated as  $T_c = \left( \frac{1}{B_0} \right)^{1/\alpha}$ . These values are presented in Table 1, using  $B_0 = 4.28 \times 10^{-7} K^{-2.49}$ ,  $7.54 \times 10^{-4} K^{1.22}$ , and  $1.11 \times 10^{-7} K^{2.71}$  for samples M1, M2, and M3, respectively. The results are in good agreement with those expected for  $\text{La}_{1-x}\text{Sr}_x\text{MnO}_3$  nanoparticles [42], [46], [48].

### Specific absorption rate calculations for magnetic hyperthermia

Once the structural and magnetic characterization had been performed, these results were used to study, by means of simulation, the possible applications of  $\text{La}_{0.7}\text{Sr}_{0.3}\text{MnO}_3$  nanoparticles in magnetic hyperthermia. As explained elsewhere, if the magnetic properties and the size distribution are known, it is possible to numerically simulate the SAR [7], [49]. One of the most important biomedical applications of magnetic nanoparticles is magnetic hyperthermia (MH).

In MH, a set of magnetic nanoparticles is submerged in a radiofrequency (RF) magnetic field. These nanoparticles absorb energy from the field and dissipate it to the medium as heat. This heat can be used to kill cancer cells. The key

parameter to measure nanoparticles' ability to transduce magnetic energy into heat is the SAR. Said heat is produced by magnetic relaxation processes governed by the imaginary part of the magnetic susceptibility ( $\chi''$ ). Thus, the SAR can be modeled as follows:

$$\text{SAR} = \mu_0 \pi f H_0^2 \int_0^\infty \chi''(f, \tau) g(\tau) d\tau \quad (6)$$

where  $\mu_0 = 4\pi \times 10^{-7}$  H/m is the vacuum magnetic permeability;  $f$  and  $H_0$  are the RF field frequency and amplitude, respectively;  $g(\tau)$  is the Gaussian distribution of the relaxation times ( $\tau$ ); and  $\chi''(f, \tau) = \frac{2\pi f \tau}{1 + (2\pi f \tau)^2} \chi_0$ , with  $\chi_0 = \frac{\mu_0 M_s^2 V}{3k_B T}$  being the low field d.c. specific susceptibility.

$\tau$  is defined as the time it takes for the magnetic moment to switch from one equilibrium position to another. If the particle is immersed in a solid matrix, a whole rotation is not allowed, and magnetic moment switching takes place internally. This is known as the Néel relaxation process. The associated relaxation time is

$$\tau = \tau_0 e^{\frac{K_{\text{eff}} V}{k_B T}} \quad (7)$$

where  $\tau_0 = 10^{-10}$  s is the characteristic time,  $K_{\text{eff}}$  is the effective magnetic anisotropy constant,  $V$  is the particle volume,  $k_B$  is the Boltzmann constant, and  $T$  is the temperature. As observed, a particle size distribution ( $g(r)$ ) generates a relaxation time distribution ( $g(\tau)$ ).

Thus, the behavior of SAR vs.  $H_0$  at 100 kHz can be calculated. The results are presented in Fig. 8.

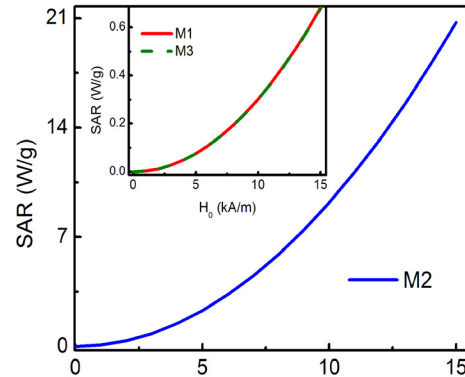


**Figure 8.** Specific absorption rate calculations vs. RF magnetic field amplitude at 100 kHz

**Source:** Authors

Moreover, the mean Néel relaxation time can be calculated: for samples M1 and M3,  $\tau \approx 0.2$  ns, and, for M2,  $\tau = 0.1$  ns. This indicates that, the lower the relaxation time, the higher the SAR.

As observed in Fig. 8, sample M2 exhibits the best SAR behavior, which means that this sample is a good candidate for biomedical applications. In addition, M2 has the highest saturation magnetization and the lowest Curie temperature.



From a chemical point of view, M2 is composed of  $\text{La}_{0.66}\text{Sr}_{0.33}\text{MnO}_3$  instead of  $\text{La}_{0.7}\text{Sr}_{0.3}\text{MnO}_3$ , the main chemical phase for samples M1 and M3. This slight increase in the Sr content enhances the magnetic properties and the SAR of M2.

## Conclusions

In this work, three different ways to synthesize  $\text{La}_x\text{Sr}_{1-x}\text{MnO}_3$  magnetic nanoparticles were tested. Although the precursors were fixed to obtain the phase  $\text{La}_{0.7}\text{Sr}_{0.3}\text{MnO}_3$ , this was only possible through the Pechini and sol-gel methods. In contrast, the ceramic method yielded the phase  $\text{La}_{0.66}\text{Sr}_{0.33}\text{MnO}_3$ . The structural characterization revealed that unreacted precursors and other manganese phases (different from  $x=0.3$  and  $x=0.33$ ) were present in all samples, implying low reaction yields, especially for the sol-gel and the ceramic methods. Meanwhile, the magnetic characterization revealed that a slight increase in Sr content leads to enhanced magnetic properties, making the sample prepared through the ceramic method (M2) a good candidate for biomedical applications, as confirmed by SAR calculations. Thus, this study demonstrated that the synthesis pathway influences the properties of LSMO nanoparticles and, consequently, their applications in magnetic hyperthermia. The results presented herein may inform improvements in the synthesis of LSMO nanoparticles for biomedical applications, especially regarding their magnetic properties. This could include magnetic hyperthermia and drug delivery. Future work is expected to address the cytotoxicity effects of LSMO nanoparticles in cell cultures and determine the heat generated in RF fields under different experimental conditions (*in vitro*, *ex-vivo*, and *in vivo*).

## Acknowledgements

We acknowledge the financial support from Universidad CESMAG (Colombia). We would like to thank Universidad de Nariño, the X-ray Laboratory of Universidad Industrial de Santander, and the Brazilian Synchrotron Light Laboratory (LNLS) for refining the physicochemical characterization of the materials.

## CRediT author statement

All authors: conceptualization, methodology, software, formal analysis, investigation, data curation, writing (original draft, review, and editing).

## Conflicts of interest

The authors of this paper declare that they have no conflicts of interest.

## References

- [1] N. D. Thorat, K. P. Shinde, S. H. Pawar, K. C. Barick, C. A. Betty, and R. S. Ningthoujam, "Polyvinyl alcohol: an efficient fuel for synthesis of superparamagnetic LSMO nanoparticles for biomedical application," *Dalt. Trans.*, vol. 41, no. 10, art. 3060, 2012. <https://doi.org/10.1039/c2dt11835a>
- [2] N. D. Thorat *et al.*, "Highly water-dispersible surface-functionalized LSMO nanoparticles for magnetic fluid hyperthermia application," *New J. Chem.*, vol. 37, no. 9, art. 2733, 2013. <https://doi.org/10.1039/c3nj00007a>
- [3] N. D. Thorat, V. M. Khot, A. B. Salunkhe, A. I. Prasad, R. S. Ningthoujam, and S. H. Pawar, "Surface functionalized LSMO nanoparticles with improved colloidal stability for hyperthermia applications," *J. Phys. D Appl. Phys.*, vol. 46, no. 10, art. 105003, Mar. 2013. <https://doi.org/10.1088/0022-3727/46/10/105003>
- [4] K. Navin and R. Kurchania, "A comparative study of the structural, magnetic transport and electrochemical properties of  $\text{La}_{0.7}\text{Sr}_{0.3}\text{MnO}_3$  synthesized by different chemical routes," *Appl. Phys. A*, vol. 126, no. 2, art. 100, Feb. 2020. <https://doi.org/10.1007/s00339-019-3269-2>
- [5] P. V. Hendriksen, S. Linderöth, and P.-A. Lindgård, "Finite-size effects in the magnetic properties of ferromagnetic clusters," *J. Magn. Magn. Mater.*, vol. 104–107, pp. 1577–1579, Feb. 1992. [https://doi.org/10.1016/0304-8853\(92\)91461-2](https://doi.org/10.1016/0304-8853(92)91461-2)
- [6] R. E. Rosensweig, "Heating magnetic fluid with alternating magnetic field," *J. Magn. Magn. Mater.*, vol. 252, pp. 370–374, 2002. [https://doi.org/http://dx.doi.org/10.1016/S0304-8853\(02\)00706-0](https://doi.org/http://dx.doi.org/10.1016/S0304-8853(02)00706-0)
- [7] M. B. Fernández van Raap, D. F. Coral, S. Yu, G. A. Muñoz, F. H. Sánchez, and A. Roig, "Anticipating hyperthermic efficiency of magnetic colloids using a semi-empirical model: A tool to help medical decisions," *Phys. Chem. Chem. Phys.*, vol. 19, no. 10, pp. 7176–7187, 2017. <https://doi.org/10.1039/C6CP08059F>
- [8] M. Soleymani, M. Edrissi, and A. Mohammad Alizadeh, "Thermosensitive polymer-coated  $\text{La}_{0.73}\text{Sr}_{0.27}\text{MnO}_3$  nanoparticles: Potential applications in cancer hyperthermia therapy and magnetically activated drug delivery systems," *Polym. J.*, vol. 47, pp. 797–801, 2015. <https://doi.org/10.1038/pj.2015.66>
- [9] B. T. Mai, S. Fernandes, P. B. Balakrishnan, and T. Pellegrino, "Nanosystems based on magnetic nanoparticles and thermo- or pH-responsive polymers: An update and future perspectives," *Acc. Chem. Res.*, vol. 51, no. 5, pp. 999–1013, May 2018. <https://doi.org/10.1021/acs.accounts.7b00549>
- [10] M. Di Marco, C. Sadun, M. Port, I. Guilbert, P. Couvreur, and C. Dubernet, "Physicochemical characterization of ultrasmall superparamagnetic iron oxide particles (USPIO) for biomedical application as MRI contrast agents," *Int. J. Nanomedicine*, vol. 2, no. 4, pp. 609–22, 2007. <http://www.ncbi.nlm.nih.gov/pubmed/18203428>
- [11] S. B. Somvanshi, P. B. Kharat, T. S. Saraf, S. B. Somvanshi, S. B. Shejul, and K. M. Jadhav, "Multifunctional nano-magnetic particles assisted viral RNA-extraction protocol for potential detection of COVID-19," *Mater. Res. Innov.*, vol. 25,

- no. 3, pp. 169–174, May 2020. <https://doi.org/10.1080/14328917.2020.1769350>
- [12] A. Jordan et al., "Presentation of a new magnetic field therapy system for the treatment of human solid tumors with magnetic fluid hyperthermia," *J. Magn. Magn. Mater.*, vol. 225, no. 1–2, pp. 118–126, Jan. 2001. [https://doi.org/10.1016/S0304-8853\(00\)01239-7](https://doi.org/10.1016/S0304-8853(00)01239-7)
- [13] C. S. S. R. Kumar and F. Mohammad, "Magnetic nanomaterials for hyperthermia-based therapy and controlled drug delivery," *Adv. Drug Deliv. Rev.*, vol. 63, no. 9, pp. 789–808, Aug. 2011. <https://doi.org/10.1016/j.addr.2011.03.008>
- [14] N. D. Thorat et al., "Superparamagnetic gadolinium ferrite nanoparticles with controllable Curie temperature-cancer theranostics for MR-imaging-guided magneto-chemotherapy," *Eur. J. Inorg. Chem.*, vol. 2016, no. 28, pp. 4586–4597, Oct. 2016. <https://doi.org/10.1002/ejic.201600706>
- [15] S. Lotfi, S. Bahari, A. Bahari, and M. Roudbari, "Magnetic performance and evaluation of radiofrequency hyperthermia of perovskite  $\text{La}_{1-x}\text{Sr}_x\text{MnO}_3$ ," *J. Supercond. Nov. Magn.*, vol. 31, no. 7, pp. 2187–2193, Jul. 2018. <https://doi.org/10.1007/s10948-017-4475-9>
- [16] T. N. Brusentsova, N. A. Brusentsov, V. D. Kuznetsov, and V. N. Nikiforov, "Synthesis and investigation of magnetic properties of Gd-substituted Mn–Zn ferrite nanoparticles as a potential low-TC agent for magnetic fluid hyperthermia," *J. Magn. Magn. Mater.*, vol. 293, no. 1, pp. 298–302, May 2005. <https://doi.org/10.1016/j.jmmm.2005.02.023>
- [17] M. H. Ehsani, P. Kameli, M. E. Ghazi, F. S. Razavi, and M. Taheri, "Tunable magnetic and magnetocaloric properties of  $\text{La}_{0.6}\text{Sr}_{0.4}\text{MnO}_3$  nanoparticles," *J. Appl. Phys.*, vol. 114, no. 22, art. 223907, Dec. 2013. <https://doi.org/10.1063/1.4846758>
- [18] R. T. Salakhova et al., "The frequency dependence of magnetic heating for  $\text{La}_{0.75}\text{Sr}_{0.25}\text{MnO}_3$  nanoparticles," *J. Magn. Magn. Mater.*, vol. 470, pp. 38–40, Jan. 2019. <https://doi.org/10.1016/j.jmmm.2017.11.126>
- [19] R. Epherre et al., "Manganite perovskite nanoparticles for self-controlled magnetic fluid hyperthermia: about the suitability of an aqueous combustion synthesis route," *J. Mater. Chem.*, vol. 21, no. 12, art. 4393, 2011. <https://doi.org/10.1039/c0jm03963b>
- [20] A. J. Campbell, G. Balakrishnan, M. R. Lees, D. McK. Paul, and G. J. McIntyre, "Single-crystal neutron-diffraction study of a structural phase transition induced by a magnetic field in  $\text{La}_{1-x}\text{Sr}_x\text{MnO}_3$ ," *Phys. Rev. B*, vol. 55, no. 14, pp. R8622–R8625, Apr. 1997. <https://doi.org/10.1103/PhysRevB.55.R8622>
- [21] P. Y. Vanina, A. A. Naberezhnov, V. I. Nizhankovskii, and R. F. Mamin, "Temperature evolution of the magnetic properties of lanthanum-strontium manganites," *St. Petersburg. Polytech. Univ. J. Phys. Math.*, vol. 2, no. 3, pp. 175–180, Oct. 2016. <https://doi.org/10.1016/j.sjpm.2016.08.001>
- [22] M. Eshraghi and P. Kameli, "Structural and magnetic properties of microwave assisted sol-gel synthesized  $\text{La}_{0.9}\text{Sr}_{0.1}\text{MnO}_3$  manganite nanoparticles," *ISRN Nanotechnol.*, vol. 2014, pp. 1–6, 2014. <https://doi.org/10.1155/2014/867139>
- [23] L. Dimesso, "Pechini processes: An alternate approach of the sol-gel method, preparation, properties, and applications," in *Handbook of Sol-Gel Science and Technology*, L. Klein, M. Aparicio, and A. Jitianu, Eds., Cham: Springer International Publishing, 2016, pp. 1–22. [https://doi.org/10.1007/978-3-319-19454-7\\_123-1](https://doi.org/10.1007/978-3-319-19454-7_123-1)
- [24] Y. Shlapa, S. Solopan, A. Belous, and A. Tovstolytkin, "Effect of synthesis method of  $\text{La}_{1-x}\text{Sr}_x\text{MnO}_3$  manganite nanoparticles on their properties," *Nanoscale Res. Lett.*, vol. 13, no. 1, art. 13, Dec. 2018. <https://doi.org/10.1186/s11671-017-2431-z>
- [25] M. Aneja, A. Tovstolytkin, and G.S. Lotey, "Superparamagnetic  $\text{LaSrMnO}_3$  nanoparticles for magnetic nanohyperthermia and their biocompatibility," *J. Magn. Magnet. Mater.*, vol. 442, pp. 423–428, 2017. <https://doi.org/10.1016/j.jmmm.2017.06.106>
- [26] N. K. Prasad, K. Rathinasamy, and D. Bahadur, " $T_c$ -tuned biocompatible suspension of  $\text{La}_{0.73}\text{Sr}_{0.27}\text{MnO}_3$  for magnetic hyperthermia," *J. Biomed. Mater. Res. Part B App. Biomater.*, vol. 85B, pp. 409–416, 2007. <https://doi.org/10.1002/jbm.b.30959>
- [27] A.B. Tewari, R. Sharma, and D. Sharma, "Magnetic hyperthermia cancer therapy using rare earth metal-based nanoparticles: An investigation of Lanthanum strontium Manganite's hyperthermic properties," *Res. Eng.*, vol. 20, art. 101537, 2023. <https://doi.org/10.1016/j.rinen.2023.101537>
- [28] T. Wang et al., "Mechanochemical effects on microstructure and transport properties of nanocrystalline  $\text{La}_{0.8}\text{Na}_{0.2}\text{MnO}_3$  ceramics," *J. Alloys Comp.*, vol. 458, no. 1–2, pp. 248–252, Jun. 2008. <https://doi.org/10.1016/j.jallcom.2007.04.023>
- [29] S. Daengsakul et al., "Magnetic and cytotoxicity properties of  $\text{La}_{1-x}\text{Sr}_x\text{MnO}_3$  ( $0 \leq x \leq 0.5$ ) nanoparticles prepared by a simple thermal hydro-decomposition," *Nanoscale Res. Lett.*, vol. 4, no. 8, pp. 839–845, Aug. 2009. <https://doi.org/10.1007/s11671-009-9322-x>
- [30] P. Kameli, H. Salamati, and A. Aezami, "Effect of particle size on the structural and magnetic properties of  $\text{La}_{0.8}\text{Sr}_{0.2}\text{MnO}_3$ ," *J. Appl. Phys.*, vol. 100, no. 5, art. 053914, Sep. 2006. <https://doi.org/10.1063/1.2345036>
- [31] P. Dey and T. K. Nath, "Enhanced grain surface effect on the temperature-dependent behavior of spin-polarized tunneling magnetoresistance of nanometric manganites," *Appl. Phys. Lett.*, vol. 87, no. 16, art. 162501, Oct. 2005. <https://doi.org/10.1063/1.2089179>
- [32] A. O. Turkey, M. M. Rashad, A. M. Hassan, E. M. Elnaggar, and M. Bechelany, "Optical, electrical and magnetic properties of lanthanum strontium manganite  $\text{La}_{1-x}\text{Sr}_x\text{MnO}_3$  synthesized through the citrate combustion method," *Phys. Chem. Chem. Phys.*, vol. 19, no. 9, pp. 6878–6886, 2017. <https://doi.org/10.1039/C6CP07333F>
- [33] J. Mera, M. Mera, C. Cordoba, O. Paredes, and O. Morán, " $\text{La}_{0.7}\text{Sr}_{0.3}\text{MnO}_3$  nanoparticles synthesized via the (Pechini) polymeric precursor method," *J. Supercond. Nov. Magn.*, vol. 26, no. 7, pp. 2553–2556, Jul. 2013. <https://doi.org/10.1007/s10948-012-1570-9>
- [34] H. A. Reshi and V. Shelke, "Grain size induced metal-insulator transition in  $\text{La}_{0.7}\text{Sr}_{0.3}\text{MnO}_3$  compounds," *J. Nano-Electron. Phys.*, vol. 5, no. 4, art. 04053, 2013. [https://jnep.sumdu.edu.ua/en/full\\_article/1131](https://jnep.sumdu.edu.ua/en/full_article/1131)
- [35] Z. Jiráček, J. Kuličková, V. Herynek, M. Maryško, J. Koktan, and O. Kaman, "Titania-coated manganite nanoparticles:

- Synthesis of the shell, characterization and MRI properties," *J. Magn. Magn. Mater.*, vol. 427, pp. 245–250, Apr. 2017. <https://doi.org/10.1016/j.jmmm.2016.10.097>
- [36] O. Glatter and O. Kratky, *Small angle x-ray scattering*. Cambridge, MA, USA: Academic Press, 1982.
- [37] J. Kohlbrecher, "SASfit: A program for fitting simple structural models to small angle scattering data," Paul Scherrer Institute, 2014. [Online]. Available: <http://kur.web.psi.ch/sans1/SANSSoft/sasfit.html>
- [38] M. H. Ehsani, M. E. Ghazi, and P. Kameli, "Effects of pH and sintering temperature on the synthesis and electrical properties of the bilayered  $\text{LaSr}_2\text{Mn}_2\text{O}_7$  manganite prepared by the sol-gel process," *J. Mater. Sci.*, vol. 47, no. 15, pp. 5815–5822, Aug. 2012. <https://doi.org/10.1007/s10853-012-6481-4>
- [39] P. Vaqueiro and M. A. López-Quintela, "Influence of complexing agents and pH on yttrium-iron garnet synthesized by the sol-gel method," *Chem. Mater.*, vol. 9, no. 12, pp. 2836–2841, Dec. 1997. <https://doi.org/10.1021/cm970165f>
- [40] A. Abreu, S. M. Zanetti, M. A. S. Oliveira, and G. P. Thim, "Effect of urea on lead zirconate titanate- $\text{Pb}(\text{Zr}_{0.52}\text{Ti}_{0.48})\text{O}_3$ -nanopowders synthesized by the Pechini method," *J. Eur. Ceram. Soc.*, vol. 25, No. 5, pp. 743–748, Feb. 2005. <https://doi.org/10.1016/j.jeurceramsoc.2004.02.021>
- [41] S. Daengsakul et al., "A simple thermal decomposition synthesis, magnetic properties, and cytotoxicity of  $\text{La}_{0.7}\text{Sr}_{0.3}\text{MnO}_3$  nanoparticles," *Appl. Phys. A*, vol. 96, no. 3, pp. 691–699, Aug. 2009. <https://doi.org/10.1007/s00339-009-5151-0>
- [42] T. Székely, G. Várhegyi, and F. Till, "The determination and use of the second derivative thermogravimetric function (DDTG) and the calculation of the kinetic constants of some decomposition reaction types," *J. Therm. Analysis*, vol. 5, pp. 227–237. 1973. <https://doi.org/10.1007/bf01950371>
- [43] J. Gaitán-Álvarez et al., "Thermogravimetric, devolatilization rate, and differential scanning calorimetry analyses of biomass of tropical plantation species of Costa Rica torrefied at different temperatures and times," *Energies*, vol. 11, art. 696 2018. <https://doi.org/10.3390/en11040696>
- [44] P. K. Yap et al., "Growth and magnetic behaviours of  $\text{La}_{0.7}\text{Sr}_{0.3}\text{MnO}_3$  nanoparticles synthesized via thermal treatment method," *Sains Malaysiana*, vol. 48, no. 2, pp. 369–375, Feb. 2019. <https://doi.org/10.17576/jsm-2019-4802-14>
- [45] H. Pfeiffer, "relaxation behaviour of magnetic particle assemblies due to thermal fluctuations," *Phys. Status Solidi*, vol. 120, no. 1, pp. 233–245, Jul. 1990. <https://doi.org/10.1002/pssa.2211200121>
- [46] C. P. Bean and J. D. Livingston, "Superparamagnetism," *J. Appl. Phys.*, vol. 30, no. 4, pp. S120–S129, 1959. <https://doi.org/10.1063/1.2185850>
- [47] D. H. Manh, P. T. Phong, P. H. Nam, D. K. Tung, N. X. Phuc, and I.-J. Lee, "Structural and magnetic study of  $\text{La}_{0.7}\text{Sr}_{0.3}\text{MnO}_3$  nanoparticles and AC magnetic heating characteristics for hyperthermia applications," *Phys. B Condens. Matter*, vol. 444, pp. 94–102, Jul. 2014. <https://doi.org/10.1016/j.physb.2014.03.025>
- [48] E. C. Stoner and E. P. Wohlfarth, "A mechanism of magnetic hysteresis in heterogeneous alloys," *Philos. Trans. R. Soc. London. Ser. A, Math. Phys. Sci.*, vol. 240, no. 826, pp. 599–642, 1948. <http://www.jstor.org/stable/91421>
- [49] J. García-Otero, A. García-Bastida, and J. Rivas, "Influence of temperature on the coercive field of non-interacting fine magnetic particles," *J. Magn. Magnet. Mater.*, vol. 189, no. 3, pp. 377–383, Nov. 1998. [https://doi.org/10.1016/S0304-8853\(98\)00243-1](https://doi.org/10.1016/S0304-8853(98)00243-1)
- [50] O. Moscoso-Londoño et al., "Different approaches to analyze the dipolar interaction effects on diluted and concentrated granular superparamagnetic systems," *J. Magn. Magnet. Mater.*, vol. 428, 2017. <https://doi.org/10.1016/j.jmmm.2016.12.019>
- [51] J.-L. Ortiz-Quiñonez, L. García-González, F. E. Cancino-Gordillo, and U. Pal, "Particle dispersion and lattice distortion induced magnetic behavior of  $\text{La}_{1-x}\text{Sr}_x\text{MnO}_3$  perovskite nanoparticles grown by salt-assisted solid-state synthesis," *Mater. Chem. Phys.*, vol. 246, art. 122834, May 2020. <https://doi.org/10.1016/j.matchemphys.2020.122834>
- [52] I. Radelytskyi et al., "Magnetic anisotropy of  $\text{La}_{0.7}\text{Sr}_{0.3}\text{MnO}_3$  nanopowders," *J. Magn. Magn. Mater.*, vol. 335, pp. 11–16, Jun. 2013. <https://doi.org/10.1016/j.jmmm.2013.01.031>
- [53] A. D Souza, P. D. Babu, S. Rayaprol, M. S. Murari, L. D. Mendonca, and M. Daivajna, "Size control on the magnetism of  $\text{La}_{0.7}\text{Sr}_{0.3}\text{MnO}_3$ ," *J. Alloys Comp.*, vol. 797, pp. 874–882, Aug. 2019. <https://doi.org/10.1016/j.jallcom.2019.05.004>
- [54] A. E. Berkowitz, W. J. Schuele, and P. J. Flanders, "Influence of crystallite size on the magnetic properties of acicular  $\gamma\text{-Fe}_2\text{O}_3$  particles," *J. Appl. Phys.*, vol. 39, no. 2, pp. 1261–1263, Feb. 1968. <https://doi.org/10.1063/1.1656256>
- [55] W. Xia, Z. Pei, K. Leng, and X. Zhu, "Research progress in rare earth-doped perovskite manganite oxide nanostructures," *Nanoscale Res. Lett.*, vol. 15, no. 1, art. 9, Dec. 2020. <https://doi.org/10.1186/s11671-019-3243-0>
- [56] P. V. Hendriksen, S. Linderöth, and P.-A. Lindgård, "Finite-size modifications of the magnetic properties of clusters," *Phys. Rev. B*, vol. 48, no. 10, pp. 7259–7273, Sep. 1993. <https://doi.org/10.1103/PhysRevB.48.7259>
- [57] D. F. Coral and J. A. Mera-Córdoba, *Nanomedicine and Nanotechnology: Magnetic Nanoparticles Applications in Cancer Treatment (Nanotecnología y Medicina: Aplicaciones de Nanopartículas Magnéticas en el Tratamiento del Cáncer)*, 1st ed. Pasto, Colombia: Editorial CESMAG, 2018. <https://doi.org/10.15658/CESMAG18.090101>